Nanoscale

RSC Publishing

PAPER

View Article Online
View Journal | View Issue

Cite this: *Nanoscale*, 2013, **5**, 7984

High energy density asymmetric supercapacitors with a nickel oxide nanoflake cathode and a 3D reduced graphene oxide anode

Feng Luan,[ab] Gongming Wang,[b] Yichuan Ling,[b] Xihong Lu,[bc] Hanyu Wang,[b] Yexiang Tong,[c] Xiao-Xia Liu*[a] and Yat Li*[b]

Received 24th May 2013
Accepted 26th June 2013

DOI: 10.1039/c3nr02710d

www.rsc.org/nanoscale

Here we demonstrate a high energy density asymmetric supercapacitor with nickel oxide nanoflake arrays as the cathode and reduced graphene oxide as the anode. Nickel oxide nanoflake arrays were synthesized on a flexible carbon cloth substrate using a seed-mediated hydrothermal method. The reduced graphene oxide sheets were deposited on three-dimensional (3D) nickel foam by hydrothermal treatment of nickel foam in graphene oxide solution. The nanostructured electrodes provide a large effective surface area. The asymmetric supercapacitor device operates with a voltage of 1.7 V and achieved a remarkable areal capacitance of 248 mF cm^{-2} (specific capacitance of 50 F g^{-1}) at a charge/discharge current density of 1 mA cm^{-2} and a maximum energy density of 39.9 W h kg^{-1} (based on the total mass of active materials of 5.0 mg). Furthermore, the device showed an excellent charge/discharge cycling performance in 1.0 M KOH electrolyte at a current density of 5 mA cm^{-2}, with a capacitance retention of 95% after 3000 cycles.

Introduction

Electrochemical capacitors (supercapacitors) with nanostructured electrodes have received increasing attention as a promising energy storage device.[1,2] They not only have a large surface area for increasing double layer capacitance, but also offer a short diffusion length for ion insertion/desertion, which is important for pseudocapacitance.[3–6] To further improve the charge transport, the development of electrodes with ordered nanostructures grown directly on a current collector without the need for polymer binders is particularly important,[5] because most polymer binders such as polyvinylidenefluoride (PVDF) and Nafion are electrochemically inactive for charge storage. Various types of nanostructured electrodes without polymer binders such as nanowire,[6] nanotube,[7,8] nanoflake,[9–11] and nanobelt[12] electrodes have been reported for use in supercapacitors. Moreover, pseudocapacitive electrode materials should be used to increase the charge storage capability of supercapacitor devices. Nickel oxide (NiO), a pseudocapacitive material, is considered to be a promising candidate for supercapacitors, due to its high theoretical specific capacitance (2584 F g^{-1}), superior reversibility and stability in alkaline solution.[13] For example, NiO single-crystalline nanoplatelets grown on a fluorine-doped tin oxide (FTO) substrate showed an areal capacitance of 64 mF cm^{-2}, and a specific capacitance of 320 F g^{-1} measured at 4 mA cm^{-2}.[9] Ordered NiO–TiO_2 nanotube arrays yielded a specific capacitance of 40 to 100 F g^{-1}.[14] Additionally, a 3D ordered Ni–NiO core–shell inverse opal electrode with an areal specific capacitance of around 10 mF cm^{-2} has been reported recently.[15] However, the small potential window (~0.5 V) of Ni limits the energy density of these Ni based electrodes. An asymmetrical supercapacitor device consisting of a battery-type Faradaic cathode and a capacitor-type anode can address this limitation by fully utilizing the potential windows of the two different electrodes. It can maximize the operation voltage of the device and effectively increase its energy density.[16,17] For example, Ganesh *et al.* reported an asymmetric supercapacitor device based on a NiO cathode and an active carbon anode,[18] and it achieved a maximum specific capacitance of 100 mF cm^{-2} (34 F g^{-1}) at a scan rate of 2 mV s^{-1}. However, the capacitance of the asymmetric device decreased drastically with the increase of the scan rate. The poor rate capability could be due to the limited ion diffusion rate. 3D nanostructured electrodes with high surface area and open space can facilitate ion diffusion that could potentially address the poor rate capability.

Here we report a high energy density asymmetric supercapacitor device with porous NiO nanoflake arrays grown on a carbon cloth substrate as the positive electrode (cathode) and reduced graphene oxide (rGO) sheets deposited on 3D nickel foam as the negative electrode (anode). This asymmetric

[a]*Department of Chemistry, Northeastern University, Shenyang, 110819, China. E-mail: xxliu@mail.neu.edu.cn*

[b]*Department of Chemistry and Biochemistry, University of California, Santa Cruz, CA 95064, USA. E-mail: yli@chemistry.ucsc.edu*

[c]*School of Chemistry and Chemical Engineering, Sun Yat-Sen University, Guangzhou, 510275, China*

supercapacitor device has a stable operational voltage of 1.7 V, and achieved an areal capacitance of 248 mF cm^{-2} (specific capacitance of 50 F g^{-1}) at a charge/discharge current density of 1 mA cm^{-2} and a maximum energy density of 39.9 W h kg^{-1} (based on the total mass of active materials of 5 mg).

Experimental section

Preparation of NiO nanoflake arrays on a carbon cloth substrate

$Ni(OH)_2$ nanoflakes were synthesized on a carbon cloth substrate (purchased from Fuel Cell Earth LLC) using a seed-mediated hydrothermal method.[19] The carbon cloth substrate was cleaned by sonication in ethanol for 30 min, and then dipped into 20 mM $Ni(NO_3)_2$ ethanol solution, followed by annealing on a hot-plate at 300 °C for 10 min. This dipping and drying cycle was repeated 5 times to obtain a seeded substrate. The seeded substrate was attached to a glass slide and was transferred into a Teflon-lined stainless steel autoclave filled with 25 ml of distilled water, 0.72 g of $Ni(NO_3)_2 \cdot 6H_2O$, 0.12 g of ammonium persulfate, and 3.12 ml of ammonium hydroxide (28%). The substrate was placed against the inner wall of the autoclave with the seeded carbon cloth facing down. The sealed autoclave was heated in an electric oven at 150 °C for 6 h and then cooled down to room temperature. The substrate was covered with a uniform cyan $Ni(OH)_2$ film. After washing with water and ethanol, and blow-dried with compressed air, the as-prepared film was annealed in air at 300 °C for 1 h to convert $Ni(OH)_2$ to NiO.

Preparation of rGO sheets on Ni foam

0.5 g of graphite powder, 20 ml of H_2SO_4 and 10 ml of HNO_3 were mixed together and cooled in an ice bath. Then 3 g of $KMnO_4$ was slowly added to the solution mixture. The solution was heated under stirring at 35 °C for 3 h and then diluted with 40 ml of distilled water. After 1.5 h, the solution was further diluted by adding an additional 100 ml of distilled water, followed by slow addition of 3.0 ml of H_2O_2 (30%). The black graphite suspensions were converted into a bright yellow graphite oxide solution. The precipitate of graphite oxide was isolated by centrifugation at 1500 rpm for 30 min, washed with distilled water, and then re-suspended in distilled water. The aqueous graphite oxide solution was sonicated vigorously for 2 h to exfoliate the stacked graphite oxide sheets into monolayer or multi-layered graphene oxide sheets. The concentration of prepared graphene oxide solution is about 2 mg ml^{-1}.

rGO sheets were deposited on a 3D nickel foam substrate by a hydrothermal method. A piece of nickel foam was first dipped into graphene oxide solution under sonication for 10 min. Then, it was placed into a Teflon-lined stainless steel autoclave filled with 25 ml of graphene oxide solution, and then heated at 180 °C for 5 h. During the heating process, graphene oxide will be reduced to rGO sheets and deposited on Ni foam. The autoclave was cooled down to room temperature. The metallic color of nickel foam became uniformly black. We repeated the hydrothermal treatment to increase the mass loading of rGO sheets on nickel foam.

Materials characterization

The electrode materials were characterized by field emission scanning electron microscopy (FE-SEM, JSM-6330F) and transmission electron microscopy (TEM, JEM2010-HR, 200 kV). The phase and composition of the samples were investigated *via* X-ray diffraction (XRD, Bruker, D8 ADVANCE) with Cu Kα radiation (λ = 1.5 418 Å) and X-ray Photoelectron Spectroscopy (XPS, ESCALab250, Thermo VG) with 200 W Al KR radiation in twin anode. For the XPS spectra, the binding energy was calibrated using the C1s photoelectron peak at 284.6 eV as the reference.

Cyclic voltammetry (CV) and galvanostatic charge/discharge curves were measured in a conventional three-electrode cell using a CHI 660D electrochemical workstation. NiO and rGO electrodes with a surface area of about 1.0 cm^2 were used as the working electrode. An Ag/AgCl (1.0 M KCl) electrode and a Pt plate of about 4.0 cm^2 were used as the reference and counter electrode, respectively. The loading amount of NiO was 2.70 mg cm^{-2}. It was determined by subtracting the weight of the carbon cloth substrate. The loading amount of rGO was determined to be 1.60 mg cm^{-2}, by dissolving the nickel foam substrate in HCl solution. The rGO precipitates were filtered under reduced pressure and collected to measure the weight. All electrochemical measurements were performed in a 1.0 M KOH aqueous solution at room temperature.

Fabrication of asymmetric supercapacitor devices

Asymmetric supercapacitor devices were assembled with NiO as the cathode and rGO as the anode. The electrodes were separated by a filter paper. The electrochemical properties of the asymmetric supercapacitor devices were measured using a CHI 660D electrochemical workstation.

Results and discussion

NiO nanoflakes were grown on the carbon cloth substrate by a seed-mediated hydrothermal method (Experiment section). XRD data collected for the as-prepared film grown on a carbon cloth showed characteristic diffraction peaks of β-$Ni(OH)_2$ (PCPDs#: 14-0117) (Fig. 1a). The presence of sharp diffraction peaks and absence of other impurity peaks suggest that the β-$Ni(OH)_2$ film has high crystallinity and purity. Upon calcination in air at 300 °C for 1 h, the characteristic diffraction peaks of β-$Ni(OH)_2$ disappeared, accompanied by the emergence of new peaks that can be indexed to cubic NiO (PDF#47–1049). These results supported the complete transformation of $Ni(OH)_2$ into NiO. SEM images were collected for the NiO film on the carbon cloth substrate. As shown in Fig. 1b, the carbon fibers of the carbon cloth substrate were uniformly covered with vertically aligned NiO nanoflakes. The thickness of each nanoflake is around 100 nm. The direct growth of NiO nanoflakes on a conductive substrate avoids the use of polymer binders such as PVDF or Nafion. We further employed TEM to study the morphology and structure of NiO nanoflakes. The TEM image revealed that NiO nanoflakes have a porous structure (Fig. 1c). The formation of the porous structure is believed to be due to the rapid dehydration of $Ni(OH)_2$.[19] The porous structure with

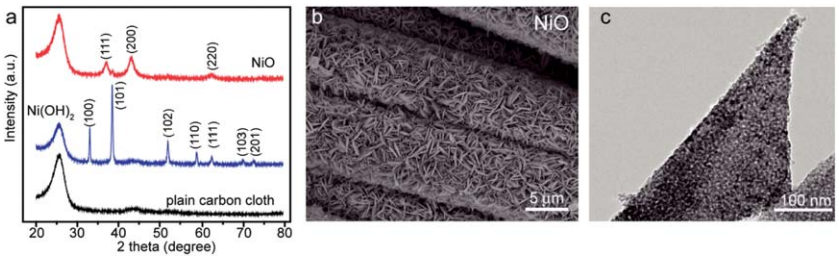

Fig. 1 (a) XRD diffraction patterns of a plain carbon cloth substrate, as-prepared $Ni(OH)_2$ film before and after post annealing. (b) SEM image of NiO nanoflakes grown on a carbon cloth. (c) TEM image collected at the edge of a porous NiO nanoflake.

an increased ion accessible surface area is indeed favorable for improving the electrochemical performance of the NiO electrode.

Cyclic voltammetry and galvanostatic charge/discharge measurements were carried out for a NiO nanoflake-arrayed electrode in 1.0 M KOH aqueous solution. Cyclic voltammograms collected at the scan rates between 5 and 50 mV s^{-1} showed distorted rectangular shapes (Fig. 2a), which is consistent with pseudocapacitive behavior of NiO. Likewise, galvanostatic charge/discharge profiles obtained at different charge/discharge current densities also show a non-linear profile, as expected for the pseudocapacitive electrode. Moreover, the charge/discharge curves are symmetric, indicating excellent reversibility and coulombic efficiency. The specific capacitances of the NiO electrode were calculated based on their galvanostatic charge/discharge curves collected at different current densities, according to eqn (1) and (2):

$$C_m = I \times \Delta t/(\Delta E \times m) \quad (1)$$

$$C_S = I \times \Delta t/(\Delta E \times S) \quad (2)$$

where C_m (F g^{-1}) is the specific capacitance, I and Δt are the charge/discharge current density and time, respectively, ΔE is the potential window, and m is the mass loading of NiO, C_S (mF cm^{-2}) is the areal specific capacitance, and S is the projected area of the electrode. The porous NiO nanoflake-arrayed electrode achieved a remarkable areal capacitance of 1054 mF cm^{-2} (specific capacitance: 392 F g^{-1}) at a relatively high mass loading of 2.7 mg cm^{-2} at a current density of 0.5 mA cm^{-2}. This areal capacitance is orders of magnitude higher than the values recently reported for NiO nanoplatelet arrays on FTO glass (less than 64 mF cm^{-2})[9] and NiO–Ni core–shell inverse opals (10 mF cm^{-2}).[15] While the specific capacitance (392 F g^{-1}) of the porous NiO electrode is smaller than the previously reported value for electrochemically prepared NiO on a 3D-carbon nanotube film substrate (1701 F g^{-1}), notably that the mass loading of NiO in this work is two orders of magnitude higher than the amount of NiO (20 μg cm^{-2}) used in the previous work.[20] High mass loading of the active material is desirable for practical application. Fig. 2c shows the calculated specific capacitances at different charge/discharge current densities (without *IR* compensation). When the current density increased from 0.5 mA cm^{-2} to 5 mA cm^{-2} about 59% of the initial capacitance was retained, indicating that the NiO electrode exhibits a good rate capability. The excellent capacitance and rate capability of the NiO electrode can be attributed to its unique structural features. First, the porous nanoflake-arrayed structure provides a large ion accessible area and facilitates ion diffusion and insertion/desertion. Second, the direct contact between NiO and carbon fibers ensures effective charge transport between NiO and the conductive substrate.

Negative electrodes (anodes) were prepared by depositing rGO sheets on 3D nickel foam by hydrothermal treatment of Ni foam in a GO solution at 180 °C for 5 h (Experimental section). SEM images revealed that the Ni foam has a 3D micro-porous structure with a smooth surface (Fig. 3a). After being hydrothermally treated in GO solution, the color of entire Ni foam changed from metallic silver to black (Fig. 3 insets), which is consistent with the color of rGO. SEM analysis further confirmed that the Ni foam was covered with aggregates of rGO sheets (Fig. 3b). A transmission electron microscopy (TEM) image was collected for rGO sheets that deposited on the nickel foam. The rGO/Ni foam structure was vigorously sonicated in ethanol solution to re-disperse the rGO sheets into the solution.

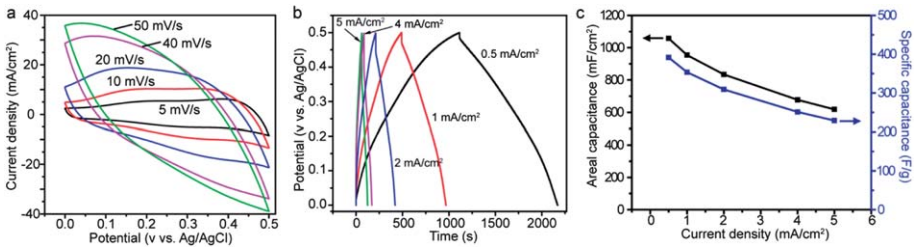

Fig. 2 (a) CV curves of the NiO electrode collected at various scan rates. (b) Galvanostatic charge/discharge curves of the NiO electrode collected at different current densities. (c) Areal capacitance and specific capacitance of the NiO electrode calculated based on galvanostatic charge/discharge curves measured at various current densities.

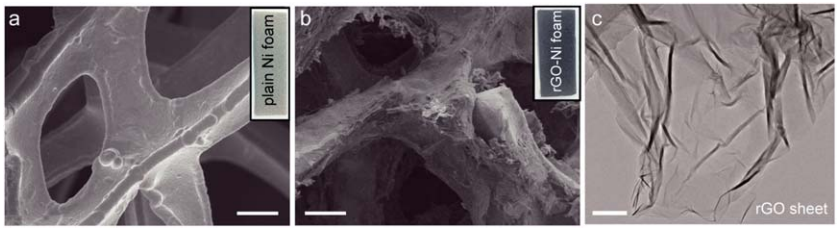

Fig. 3 SEM images of (a) plain Ni foam and (b) rGO decorated Ni foam. Scale bars are 50 μm. Insets: digital pictures of plain Ni foam and rGO decorated Ni foam. (c) TEM image of rGO sheets collected from the rGO/Ni foam electrode. Scale bar is 200 nm.

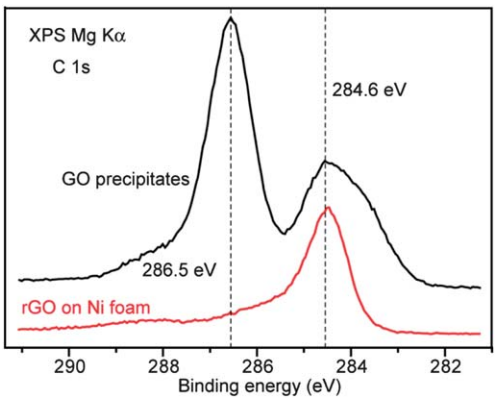

Fig. 4 Core level C 1s XPS spectra collected for GO precipitates and rGO sheets deposited on Ni foam.

The solution was then transferred to the lacey carbon coated copper grid for TEM imaging. Fig. 3c shows a representative TEM image of the rGO sheet obtained from the rGO/Ni electrode. The results support the successful deposition of rGO sheets on Ni foam. To confirm the formation of rGO, core level XPS C1s spectra were collected for GO precipitates and the rGO/Ni foam electrode. As shown in Fig. 4, the GO sample exhibited two peaks centered at binding energies of 284.6 eV and 286.5 eV. These C 1s signals are the characteristic binding energies for graphitic C=C and C–O species, respectively.[21] This is expected for GO sheets, in which the graphene sheets are modified with oxygen-containing functional groups. Most importantly, the XPS results revealed that the hydrothermally treated GO sheets have a substantially reduced C–O signal (286.5 eV), suggesting that most of the surface oxygen containing groups have been reduced.

Cyclic voltammograms collected for the rGO electrode at different scan rates showed quasi-rectangular shapes, suggesting that the electrode has excellent electrochemical double layer capacitance (Fig. 5a). Moreover, the charge/discharge curves are symmetric and linear, again proving the good reversibility and double layer capacitive behavior of rGO (Fig. 5b). Fig. 5c shows the calculated areal capacitance and specific capacitance of the rGO electrode as a function of charge/discharge current density. The areal capacitance and specific capacitance at a charge/discharge current density of 5 mA cm^{-2} (3.1 A g^{-1}) were calculated to be 370 mF cm^{-2} and 210 F g^{-1}, which are comparable to those of previously reported thermally reduced graphene (264 F g^{-1} at 100 mA g^{-1}),[22] highly corrugated graphene sheets (227 F g^{-1} at 1 A g^{-1}),[23] and the low-temperature reduced graphene oxide (260.5 F g^{-1} at 0.4 A g^{-1}).[24]

An asymmetric supercapacitor device was assembled by using a NiO nanoflake as the cathode and rGO as the anode (denoted as NiO//rGO) (Fig. 6a). As shown in Fig. 6b, by combining the NiO cathode and rGO anode, charge can be stored in a potential window between +0.5 and −1.2 V *vs.* Ag/AgCl. Therefore, the NiO//rGO device could achieve a maximum working voltage of 1.7 V. To achieve the maximum device capacitance, according to the equation $1/C_{total} = 1/C_{cathode} + 1/C_{anode}$, the charge storage capacity of both positive and negative electrodes should be balanced. Since the specific capacitances and operation potential window of NiO and rGO are different, their charge storage capacities were balanced by adjusting the mass loading between these two electrodes. The NiO to rGO mass ratio was calculated by the following equation to achieve a charge balance ($q^+ = q^-$).

$$m_+/m_- = (C_- \times \Delta E_-)/(C_+ \times \Delta E_+) \quad (3)$$

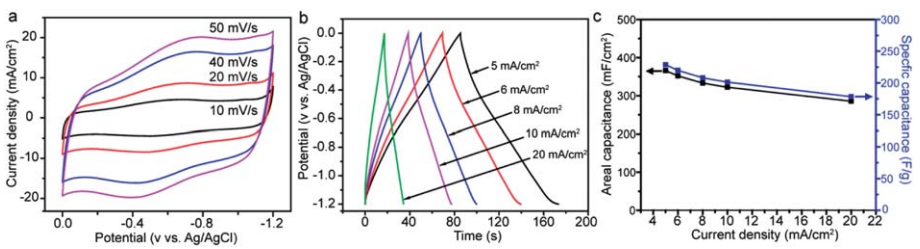

Fig. 5 (a) CV curves of the rGO electrode collected at various scan rates. (b) Galvanostatic curves of the rGO electrode collected at different charge/discharge current densities. (c) Areal capacitance and specific capacitance of the rGO electrode calculated based on galvanostatic charge/discharge curves measured at various current densities.

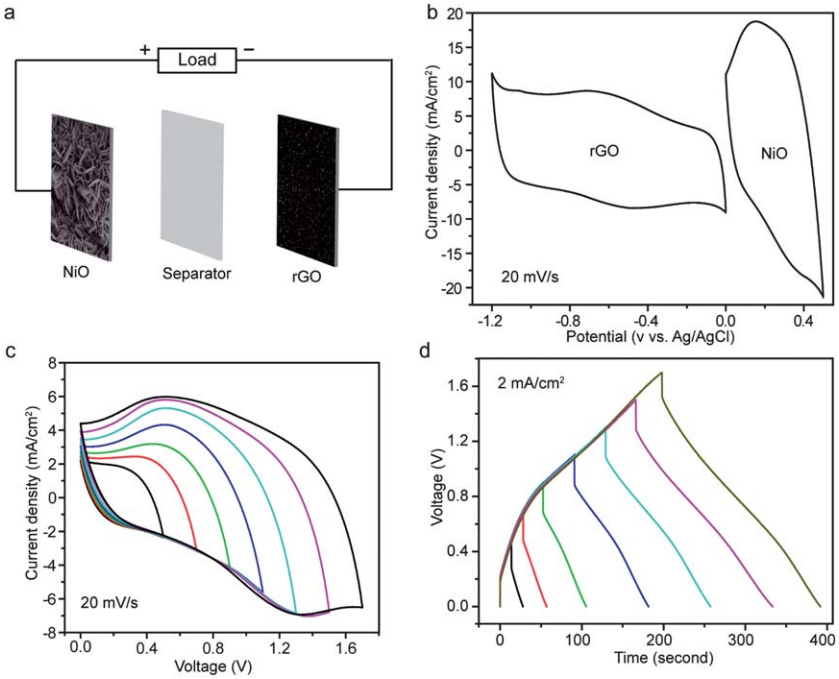

Fig. 6 (a) Schematic illustration of the asymmetric supercapacitor device composed of the NiO cathode and rGO anode. The two electrodes are separated by a filter paper (separator). (b) CV curves of NiO and rGO electrodes collected at a scan rate of 20 mV s^{-1} in a three-electrode system. (c) CV curves of the asymmetric supercapacitor device collected at different voltages at a scan rate of 20 mV s^{-1}. (d) Galvanostatic charge/discharge curves of the asymmetric supercapacitor device collected at different voltages at a fixed current density of 2 mA cm^2.

where q^+, q^-, m_+, m_-, C_+, C_-, E_+, and E_- are the charge, mass, specific capacitance and potential windows obtained in the three-electrode measurement for the cathode (+) and anode (−). The NiO to rGO mass ratio was adjusted to be 2.4 : 1.

Fig. 6c shows the CV curves of a NiO//rGO asymmetric supercapacitor device (two electrode system) collected at different working voltages at a scan rate of 20 mV s^{-1}. The data proved that the device can operate within the voltage range of

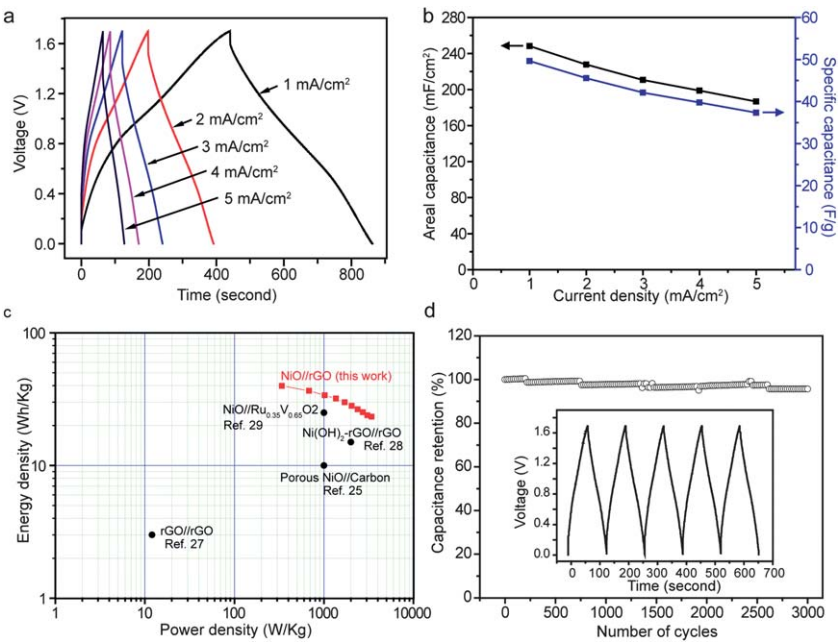

Fig. 7 (a) Galvanostatic charge/discharge curves of the NiO//rGO asymmetric device collected at different current densities. (b) Areal capacitance and specific capacitance of the device calculated as a function of the current density based on galvanostatic charge/discharge curves. (c) Ragone plot of the device. Energy and power density of other previously reported asymmetric supercapacitor devices are added as references. (d) Cycling performance of the device measured at a current density of 5 mA cm^{-2}. Inset: galvanostatic charge/discharge curves of the device measured at a current density of 5 mA cm^{-2}.

1.7 V. The distorted rectangular CV curves were attributed to the contribution from the NiO pseudocapacitive cathode. The symmetric charge/discharge curves indicated that the device exhibits good capacitive behavior in the entire range of working voltage from 0.5 to 1.7 V (Fig. 6d). These asymmetric supercapacitor devices exhibited an *IR* drop, which could be due to the relatively high resistance of the NiO cathode.

Fig. 7a shows the galvanostatic charge/discharge profiles of the asymmetric supercapacitor collected at the current densities from 1 to 5 mA cm^{-2}. The device exhibited symmetric charge/discharge curves, suggestive of a good charge storage performance. The NiO//rGO device achieved a remarkable areal capacitance of 248 mF cm^{-2} (specific capacitance of 50 F g^{-1}) at a current density of 1 mA cm^2. The areal capacitance is substantially higher than the value previously reported for the asymmetric capacitor device based on the NiO cathode and activated carbon anode (100 mF cm^{-2} or 34 F g^{-1} measured at a scan rate of 2 mV s^{-1}).[18] The specific capacitance of 50 F g^{-1} (with a total mass loading of active material of 5 mg) is comparable to the reported values for asymmetric capacitor devices based on hierarchical porous NiO//porous carbon (38 F g^{-1})[25] and NiO//activated carbon with an alkaline polymer gel electrolyte (73.4 F g^{-1}),[26] which have lower mass loading of active materials.

The energy density (E_s) and power density (P_s) of the asymmetric supercapacitor were calculated by the following equations:

$$E_s = 1/2 C_s U^2 \quad (4)$$

$$P_s = 3600 E_s/t \quad (5)$$

where C_s is the specific capacitance calculated based on the mass loading of active materials on both electrodes, U is the operating voltage of the cell and t is the discharge time. Fig. 7c shows the Ragone plot of the NiO//rGO supercapacitor devices. The device achieved a maximum energy density of 39.9 W h kg^{-1}. This energy density is substantially higher than the values reported for the rGO//rGO symmetric supercapacitor device,[27] and it is slightly higher than those of the asymmetric supercapacitor devices such as hierarchical porous NiO//carbon,[25] $Ni(OH)_2$–rGO//rGO,[28] and NiO//$Ru_{0.35}V_{0.65}O_2$ devices.[29] Furthermore, the charge/discharge cycling performance of the NiO//rGO device was tested at an operating voltage of 1.7 V at a current density of 5 mA cm^{-2}. Significantly, the asymmetric supercapacitor device exhibited an excellent cycling performance with 95% specific capacitance retention after 3000 cycles (Fig. 7d). This retention rate is also better than the values reported for NiO based asymmetric devices, including NiO//activated carbon (93% after 800 cycles),[26] NiO//$Ru_{0.35}V_{0.65}O_2$ (83.5% after 1500 cycles),[29] and porous NiO//carbon devices (50% after 1000 cycles).[25]

Conclusion

We have demonstrated an asymmetric supercapacitor device composed of a porous NiO nanoflake-arrayed cathode and an rGO anode. By coupling the cathode and anode, the device can operate at an operating voltage of 1.7 V. The device achieved a remarkable areal capacitance of 248 mF cm^{-2} and a high energy density of 39.9 W h kg^{-1} with a high mass loading of 5 mg active materials. The enhanced charge storage performance is believed to be due to the increased surface area of the porous NiO nanoflake and rGO sheets. This work demonstrates the potential of nanostructured NiO electrodes for use in asymmetric supercapacitor devices.

Acknowledgements

X.-X. Liu gratefully acknowledges financial supports from the National Natural Science Foundation of China (21273029) and Research Foundation for Doctoral Program of Higher Education of China (20120042110024). Y. Li. acknowledges the support of this work by UCSC new faculty start up fund and NSF CAREER award (DMR-0847786). Y. X. Tong acknowledges the financial support of this work by the Natural Science Foundation of China (90923008 and 21273290). G. M. Wang thanks the financial support of Chancellor's Dissertation Year Fellowship. F. Luan and X. H. Lu thank the China Scholarship Council for financial support.

Notes and references

1 J. R. Miller and P. Simon, *Science*, 2008, **321**, 651–652.
2 P. Simon and Y. Gogotsi, *Nat. Mater.*, 2008, **7**, 845–854.
3 H. L. Wang, H. S. Casalongue, Y. Y. Liang and H. J. Dai, *J. Am. Chem. Soc.*, 2010, **132**, 7472–7477.
4 H. Jiang, C. Z. Li, T. Sun and J. Ma, *Chem. Commun.*, 2012, **48**, 2606–2608.
5 J. F. Xie, X. Sun, N. Zhang, K. Xu, M. Zhou and Y. Xie, *Nano Energy*, 2013, **2**, 65–74.
6 J. X. Li, M. Yang, J. P. Wei and Z. Zhou, *Nanoscale*, 2012, **4**, 4498–4503.
7 X. H. Lu, G. M. Wang, T. Zhai, M. H. Yu, J. Y. Gan, Y. X. Tong and Y. Li, *Nano Lett.*, 2012, **12**, 1690–1696.
8 J. H. Chen, W. Z. Li, D. Z. Wang, S. X. Yang, J. G. Wen and Z. F. Ren, *Carbon*, 2002, **40**, 1193–1197.
9 J. T. Li, W. Zhao, F. Q. Huang, A. Manivannan and N. Q. Wu, *Nanoscale*, 2011, **3**, 5103–5109.
10 Z. Endut, M. Hamdi and W. J. Basirun, *Thin Solid Films*, 2013, **528**, 213–216.
11 Z. P. Li, Y. J. Mi, X. H. Liu, S. Liu, S. R. Yang and J. Q. Wang, *J. Mater. Chem.*, 2011, **21**, 14706–14711.
12 X. J. Zhang, L. T. Yu, L. L. Wang, R. Ji, G. F. Wang and B. Y. Geng, *Phys. Chem. Chem. Phys.*, 2013, **15**, 521–525.
13 G. Q. Zhang, L. Yu, H. E. Hoster and X. W. Lou, *Nanoscale*, 2013, **5**, 877–881.
14 J. H. Kim, K. Zhu, Y. F. Yan, C. L. Perkins and A. J. Frank, *Nano Lett.*, 2010, **10**, 4099–4104.
15 J. H. Kim, S. H. Kang, K. Zhu, J. Y. Kim, N. R. Neale and A. J. Frank, *Chem. Commun.*, 2011, **47**, 5214–5216.
16 X. Xiao, T. P. Ding, L. Y. Yuan, Y. Q. Shen, Q. Zhong, X. H. Zhang, Y. Z. Cao, B. Hu, T. Zhai, L. Gong, J. Chen,

Y. X. Tong, J. Zhou and Z. L. Wang, *Adv. Energy Mater.*, 2012, **2**, 1328–1332.
17 X. H. Lu, M. H. Yu, G. M. Wang, T. Zhai, S. L. Xie, Y. C. Ling, Y. X. Tong and Y. Li, *Adv. Mater.*, 2013, **25**, 267–272.
18 V. Ganesh, S. Pitchumani and V. Lakshminarayanan, *J. Power Sources*, 2006, **158**, 1523–1532.
19 G. M. Wang, X. H. Lu, T. Zhai, Y. C. Ling, H. Y. Wang, Y. X. Tong and Y. Li, *Nanoscale*, 2012, **4**, 3123–3127.
20 K. W. Nam, K. H. Kim, E. S. Lee, W. S. Yoon, X. Q. Yang and K. B. Ki, *J. Power Sources*, 2008, **182**, 642–652.
21 J. I. Paredes, S. Villar-Rodil, A. Martinez-Alonso and J. M. D. Tascon, *Langmuir*, 2008, **24**, 10560–10564.
22 W. Lv, D. M. Tang, Y. B. He, C. H. You, Z. Q. Shi, X. C. Chen, C. M. Chen, P. X. Hou, C. Liu and Q. H. Yang, *ACS Nano*, 2009, **3**, 3730–3736.
23 J. Yan, J. P. Liu, Z. J. Fan, T. Wei and L. J. Zhang, *Carbon*, 2012, **50**, 2179–2188.
24 B. Zhao, P. Liu, Y. Jiang, D. Y. Pan, H. H. Tao, J. S. Song, T. Fang and W. W. Xu, *J. Power Sources*, 2012, **198**, 423–427.
25 D. W. Wang, F. Li and H. M. Cheng, *J. Power Sources*, 2008, **185**, 1563–1568.
26 C. Z. Yuan, X. G. Zhang, Q. F. Wu and B. Gao, *Solid State Ionics*, 2006, **177**, 1237–1242.
27 J. T. Zhang, J. W. Jiang, H. L. Li and X. S. Zhao, *Energy Environ. Sci.*, 2011, **4**, 4009–4015.
28 J. Yan, Z. J. Fan, W. Sun, G. Q. Ning, T. Wei, Q. Zhang, R. F. Zhang, L. J. Zhi and F. Wei, *Adv. Funct. Mater.*, 2012, **22**, 2632–2641.
29 C. Z. Yuan, B. Gao and X. G. Zhang, *J. Power Sources*, 2007, **173**, 606–612.